

Statistical analysis of barren plateaus in variational quantum algorithms

Le Bin Ho,^{1,2,*} Jesus Urbaneja,³ and Sahel Ashhab^{4,5}

¹*Frontier Research Institute for Interdisciplinary Sciences, Tohoku University, Sendai 980-8578, Japan*

²*Department of Applied Physics, Graduate School of Engineering, Tohoku University, Sendai 980-8579, Japan*

³*Department of Mechanical and Aerospace Engineering, Tohoku University, Sendai 980-0845, Japan*

⁴*Advanced ICT Research Institute, National Institute of Information and Communications Technology (NICT), 4-2-1, Nukui-Kitamachi, Koganei, Tokyo 184-8795, Japan*

⁵*Research Institute for Science and Technology, Tokyo University of Science, 1-3 Kagurazaka, Shinjuku-ku, Tokyo 162-8601, Japan*

(Dated: August 13, 2025)

We investigate the barren plateau (BP) phenomenon in variational quantum algorithms using a statistical approach. Using Gaussian function models, we identify three distinct types of BPs. The first type, which we called localized-dip BPs, occurs in landscapes that are mostly flat but contain a dip point where the gradient is large in a small region around the minimum. The second type, called localized-gorge BPs, which are somewhat similar to the localized-dip BPs but contain a gorge line. The third type, called everywhere-flat BPs, appears when the entire landscape is uniformly flat with almost vanishing gradients, making optimization significantly more difficult. After illustrating these behaviors in the Gaussian function models, we extend the analysis to the variational quantum eigensolver (VQE). We consider two types of ansätze: the hardware-efficient ansatz and the random Pauli ansatz. For both ansätze, we only observe the everywhere-flat BPs. Using our statistical approach, we searched for localized-dip and localized-gorge BPs but found no evidence of such features in the examples studied, suggesting that everywhere-flat BPs dominate in these ansätze. Our method effectively probes landscape features by capturing the gradient scaling across parameter space, making it a useful tool for diagnosing BPs in variational algorithms. To mitigate BPs in the VQE, we employ a genetic algorithm (GA) to optimize the random gates generated in the ansätze, thereby reshaping the cost function landscape to enhance the optimization efficiency. A comparison with an unoptimized ansatz shows how the ansatz design can improve the scalability and reliability of variational quantum algorithms.

I. INTRODUCTION

Variational quantum algorithms (VQAs) are central to the development of quantum computing on near-term hardware. By combining parameterized quantum circuits with classical optimization, VQAs offer a flexible framework for tackling a wide range of problems in quantum chemistry, machine learning, and many-body physics [1]. Their compatibility with noisy intermediate-scale quantum (NISQ) devices makes them particularly attractive for practical implementation in the near future.

However, a major limitation in scaling VQAs is the barren plateau (BP) phenomenon [2], which refers to the exponential vanishing of cost function gradients with increasing system complexity. This phenomenon occurs when the cost function landscape becomes extremely flat, hindering numerical optimizers from finding the optimal direction for improvement with gradient-based methods.

BPs are influenced by the structure of the parameterized quantum circuits (ansätze) and the choice of cost functions, which include random t -design ansatz [2, 3], ansatz expressibility [4, 5], global cost functions and cost function concentration [3, 6, 7], noise [8] and entangled ansatz [9]. Recently, these sources of BPs have been unified under a common framework based on Lie algebra

theory [10, 11], which provides a deeper understanding of their origin.

To mitigate BPs, several strategies have been proposed, including engineered parameter initialization [12–14], low-entanglement circuit initializations [15], shallow circuit designs [3], classical shadows [16], local cost functions [3], transferability of smooth solutions [17], pre-training [18–21], and engineered dissipation [22]. These approaches aim to preserve gradients and enhance trainability.

Previous studies have primarily examined BPs in specific circuit architectures or initialization schemes, using analytical tools and numerical simulations [2–11]. While these works identify when and where BPs occur, they do not address the possible differences between different types of BPs. Understanding the statistical properties of BPs can provide insight into different possible scenarios and can help guide the development of strategies to effectively mitigate the deleterious effects of BPs.

In this work, we introduce a statistical framework to explain the origins of BPs by analyzing the cost function landscape and its distribution in parameter space. We identify three distinct types: one where the landscape is flat almost everywhere but contains a sharp dip with a steep slope, one that contains a sharp gorge, and one where the landscape is uniformly smooth and flat.

We analyze gradient behavior using example models of Gaussian functions, which exhibits these types of BPs. We then extend the analysis to VQE models with

* Electronic address: binho@fris.tohoku.ac.jp

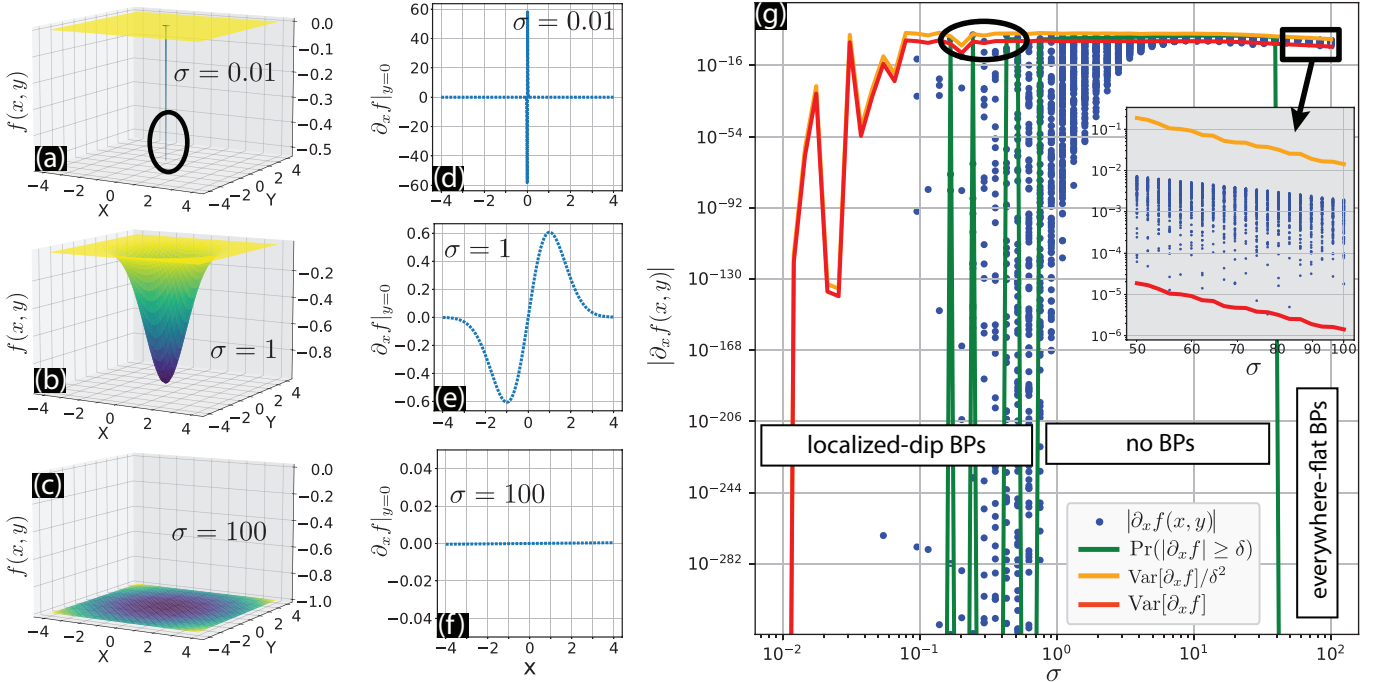


FIG. 1. (a–c) 3D plots of the isotropic Gaussian function $f(x, y)$ in Eq. (1) for different values of σ . The landscapes in (a) and (c) are mostly flat, except for a deep peak in (a), highlighted by the black oval. (d–f) Derivatives of the Gaussian function $\partial_x f|_{y=0}$ plotted against x with $y = 0$. (g) Plot of the statistical distribution of the derivatives $|\partial_x f|$, the threshold probability $\Pr(|\partial_x f| \geq \delta)$, the Chebyshev bound $\text{Var}[\partial_x f]/\delta^2$ for $\delta = 0.01$, and corresponding variance $\text{Var}[\partial_x f]$. The probability $\Pr(|\partial_x f| \geq \delta)$ divides the derivatives into three regions, with BPs appearing in the first and third regions. In the localized-dip plateau region, certain parameter sets (x, y) avoid BPs by falling within the dip point, marked by the black oval in PBs. Inset: A zoom-in of the everywhere-flat region with $\sigma \in [50, 100]$, illustrating the exponential decay of the derivatives, while showing that the distribution's width on a logarithmic scale depends only weakly on σ .

the hardware-efficient ansatz (HEA) and random Pauli ansatz (RPA). We find that these ansätze are dominated by everywhere-flat plateaus.

We then propose a mitigation strategy using a genetic algorithm [23] to eliminate BPs by optimizing the random gates generated in the ansatz, thereby reshaping the cost function landscape and enhancing its gradients for more effective optimization. This study presents a statistical perspective on BPs and provides a practical solution to improve the scalability and reliability of VQAs.

The rest of the paper is organized as follows. In Section II, we present the statistical analysis of BPs in the Gaussian function models, and in Section III, we focus on VQE. Section IV details the proposed mitigation strategy and its application to quantum circuits. We conclude in Section V with a discussion of implications and future directions.

II. BPS IN MODEL FUNCTIONS

In this section, we investigate the statistical behavior under different geometrical plateau profiles, specifically narrow dip/gorge and flat structures, using simple 2D Gaussian functions as examples. We use two Gaussian

functions: an isotropic 2D Gaussian with equal standard deviations in both directions, and an anisotropic 2D Gaussian with different standard deviations along x and y .

A. Isotropic 2D Gaussian

We begin by examining an isotropic 2D Gaussian function as a cost function and its derivative with respect to x

$$f(x, y) = -\exp\left(-\frac{x^2 + y^2}{2\sigma^2}\right), \quad (1)$$

where σ is the standard deviation. The derivative with respect to x gives

$$\frac{\partial f(x, y)}{\partial x} = \frac{x}{\sigma^2} \exp\left(-\frac{x^2 + y^2}{2\sigma^2}\right). \quad (2)$$

Figure 1(a–c) shows $f(x, y)$ for three values of σ . For very small σ , e.g., $\sigma = 0.01$, it is flat except for a sharp dip centered at $x = y = 0$, marked by the black oval in Fig. 1(a). The corresponding derivative $\partial f/\partial x|_{y=0}$, shown in Fig. 1(d), is almost zero everywhere except for

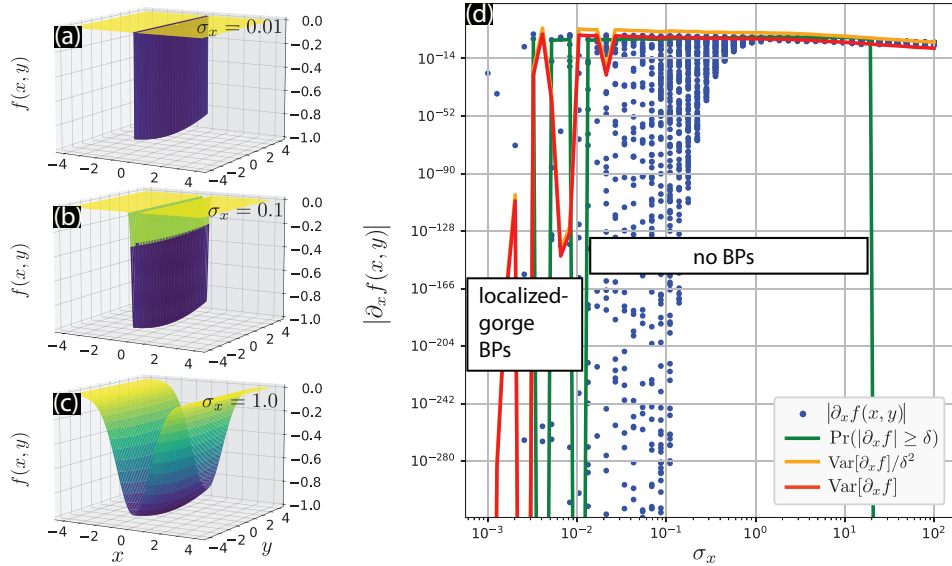


FIG. 2. (a–c) 3D plots of the anisotropic Gaussian function $f(x, y)$ in Eq. (4) for various values of σ_x , with $\sigma_y = 10$. In (a), the landscape is mostly flat except for a deep gorge along $x = 0$, in contrast to the localized dip observed in Fig. 1(a). (d) Statistical analysis of the derivatives $|\partial_x f|$, including the distribution, the threshold probability $\Pr(|\partial_x f| \geq \delta)$, the Chebyshev bound $\text{Var}[\partial_x f]/\delta^2$ with $\delta = 0.01$, and the variance $\text{Var}[\partial_x f]$, following the same procedure as in Fig. 1(g). All other parameters are the same as those in Fig. 1.

a high-peak-deep-valley structure at the dip point. This behavior indicates a BP, even though this behavior does not occur at the dip, as will be discussed later. As σ increases to moderate values (figure b), $f(x, y)$ forms a more defined shape, and $\partial f/\partial x|_{y=0}$ in Fig. 1(e) remains non-zero across a wider range of x , indicating the absence of BPs. When σ becomes large, $f(x, y)$ flattens further as shown in Fig. 1(c), and $\partial f/\partial x|_{y=0}$ vanishes everywhere as shown in Fig. 1(f), which is a characteristic feature of BPs.

The first and third cases both exhibit BPs, but the BPs in the two cases arise from different causes. For very small σ , the plateau is correlated with the development of a sharp dip at the origin, referred to as a localized-dip BP. In contrast, for large σ , the landscape is uniformly flat with no guiding features, leading to an everywhere-flat BP.

To further explore the different types of BPs, we generate random x, y values uniformly distributed in the range $[-20, 20]$ and examine the distribution of $|\partial f/\partial x|$, as shown in Fig. 1(g). The results show that for both very small and very large σ , most derivatives are close to zero. This confirms that the gradients vanish across these domains, indicating BPs. For localized-dip BPs, the derivatives become extremely small for most of the parameter space, while rare large derivatives continue to exist. In contrast, for everywhere-flat BPs, the derivatives do not decrease as dramatically, because they remain on the order of the ratio between range of cost function values and the range of variable parameter values.

To quantify this behavior, we apply Chebyshev's inequality, a statistical tool that bounds the probability of

a variable deviating from its mean

$$\Pr(|\partial_x f - \langle \partial_x f \rangle| \geq \delta) \leq \frac{\text{Var}[\partial_x f]}{\delta^2}, \quad (3)$$

where $\langle \partial_x f \rangle$ is the mean, $\text{Var}[\partial_x f]$ is the variance, and $\delta > 0$ is a chosen threshold. In many cases, the average derivative $\langle \partial_x f \rangle$ is zero due to the symmetry of the landscape.

This inequality shows that when the variance is small, the probability of observing large gradients becomes negligible. Thus, Chebyshev's inequality provides a rigorous way to detect BPs: if the variance of the gradient is low, significant deviations from the mean are unlikely, indicating an almost flat landscape.

When BPs occur, the probability $\Pr(|\partial_x f| \geq \delta)$ becomes negligible, as described by Chebyshev's inequality. This is the statistical explanation for the occurrence of flat gradients in the optimization landscape. Figure 1(g) plots $\Pr(|\partial_x f| \geq \delta)$ (green) and its Chebyshev bound $\text{Var}[\partial_x f]/\delta^2$ (orange) for $\delta = 10^{-2}$. In the central region, the inequality is violated, that is, the observed probability exceeds the bound, indicating no BP. In contrast, on the left and right sides, the probability drops to zero and satisfies the inequality, signaling a BP. However, the inequality may become loose when $\text{Var}[\partial_x f]/\delta^2 > 1$, since $\Pr(|\partial_x f| \geq \delta) \leq 1$ trivially holds. Therefore, while Chebyshev's bound helps identify BPs, its interpretability depends on how tight the bound is in each region.

Our statistical analysis suggests that in the presence of local-dip BPs, there is still a chance to reach the global minimum. For example, in the left region of Fig. 1(g), certain values of x near or at the dip point (marked by

the black oval) yield non-vanishing gradients. This indicates that local dips may provide an opportunity for optimization. This enables statistical analysis to identify such regions prior to training, rather than using random initialization. In contrast, the right region exhibits an everywhere-flat plateau, where $|\partial f/\partial x|$ decreases exponentially across the entire domain, making optimization more challenging. The inset focuses on the everywhere-flat region for $\sigma \in [50, 100]$, demonstrating the exponential decay of the derivatives and revealing that the distribution's width on a logarithmic scale depends weakly on σ .

B. Anisotropic 2D Gaussian

Next, we consider an anisotropic 2D Gaussian model, where σ differs for different parameters, i.e.,

$$f(x, y) = -\exp\left(-\frac{x^2}{2\sigma_x^2} - \frac{y^2}{2\sigma_y^2}\right). \quad (4)$$

We examine the case where σ_y is fixed (e.g., $\sigma_y = 10$, as shown in Fig. 2). The overall landscape resembles that of the isotropic case. However, as σ_x decreases, the central well progressively contracts along the x -axis, eventually forming a deep gorge, which is clearly visible in Fig. 2(a) for $\sigma_x = 0.01$. We refer to this configuration as the localized-gorge BPs.

To distinguish between the localized-dip and localized-gorge BPs, we analyze the statistical behavior in Fig. 2(d), following the same approach as in Fig. 1(g). Overall, the statistical profiles in both cases appear qualitatively similar. However, the no-plateau region (middle region) is broader than in the previous case and extends further toward smaller σ_x . Furthermore, the localized-gorge BPs emerge only when σ_x becomes significantly smaller than in the localized-dip scenario, marking a key distinction between the two cases.

This observation underscores an important point: despite the similarity in statistics along the x -direction, the overall landscape is less confined owing to the lack of contraction along the y -axis. Consequently, the localized-gorge BPs arise in an extreme parameter regime and exert a weaker influence on the training process, as they occupy a narrower region of the parameter space and have less impact on gradient suppression.

For further comparison, Fig. 3 highlights these two types of BPs. In the localized-dip case, the central well contracts uniformly in all directions, forming a sharp dip at $x = y = 0$. In contrast, the localized-gorge case exhibits contraction along the x -axis, resulting in a narrow, elongated gorge at $x = 0$.

III. BPS IN VQAS

VQAs are hybrid algorithms that combine quantum circuits with classical optimization techniques to solve

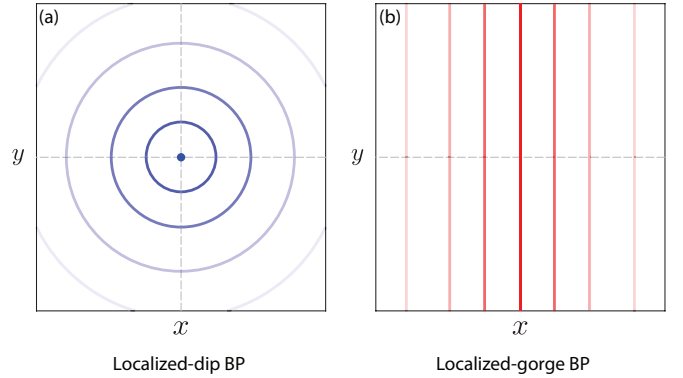


FIG. 3. Illustration of the localized-dip BP (a) and localized-gorge BP (b). (a) The central well contracts uniformly in all directions, forming a sharp dip at $x = y = 0$. (b) The central well contracts along the x -axis, resulting in a sharp gorge at $x = 0$.

complex problems. Since VQAs are based on a heuristic approach, they can be applied to any computational problem that can be posed as an optimization problem. The performance of any specific VQA then depends on the quality of the quantum circuit structure and parameter rules used by the algorithm. In these algorithms, a system evolves under a parameterized circuit $U(\boldsymbol{\theta})$, where $\boldsymbol{\theta}$ are trainable parameters. A classical optimization algorithm then iteratively updates these parameters to minimize a cost function $C(\boldsymbol{\theta})$, driving the system toward an optimal solution.

Let $\partial_{\theta_i} C \equiv \partial C / \partial \theta_i$ denote the derivative of the cost function $C(\boldsymbol{\theta})$ with respect to a parameter θ_i . In a problem that is characterized by the presence of BPs, the variance of this gradient scales as $\text{Var}(\partial_{\theta_i} C) \propto e^{-N}$, where N is the system size (e.g., the number of qubits) [2]. This exponential decay limits the effectiveness of gradient-based optimization.

Hereafter, we analyze BPs in VQAs using the statistical approach introduced in the previous section.

A. Ansätze

We examine a benchmark VQA [24] using two ansätze: the hardware-efficient ansatz (HEA) [25] and the random Pauli ansatz (RPA) [2], as illustrated in Fig. 4. The HEA is composed of a sequence of parameterized quantum gates, where the unitary operator $U(\boldsymbol{\theta})$ is typically structured as

$$U(\boldsymbol{\theta}) = \prod_{\ell=1}^L \left(U_{\text{ent}}^{(\ell)} \cdot U_{\text{rot}}^{(\ell)}(\boldsymbol{\theta}^{(\ell)}) \right), \quad (5)$$

where L is the number of layers, $U_{\text{rot}}^{(\ell)}$ includes parameterized single-qubit rotations, i.e., $U_{\text{rot}}(\boldsymbol{\theta}^{(\ell)}) = \bigotimes_{j=1}^N R_y(\theta_{j,3}^{(\ell)}) R_x(\theta_{j,2}^{(\ell)}) R_y(\theta_{j,1}^{(\ell)})$, and $U_{\text{ent}}^{(\ell)}$ represents entangling gates such as a fixed combination of CZ gates

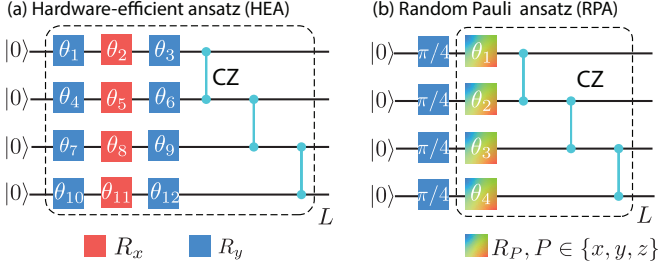


FIG. 4. Illustration of a parameterized quantum circuit with $N = 4$ qubits. (a) Hardware-efficient ansatz (HEA): The circuit starts from the initial state $|0\rangle$, followed by a sequence of R_y - R_x - R_y rotations on each qubit. Controlled-Z (CZ) gates are then applied between adjacent qubits in a linear topology. This structure is repeated over L layers. (b) Random Pauli ansatz (RPA): The circuit begins with a fixed layer of $R_Y(\pi/4)$ gates applied to all qubits, followed by L layers of randomly selected single-qubit Pauli rotations and CZ gates.

applied to the qubits. Note that the different CZ gates commute and can be implemented simultaneously. For simplicity, we rewrite $\theta_{1,1}^{(\ell=1)}$ as θ_1 ; $\theta_{1,2}^{(\ell=1)}$ as θ_2 , and so on. The total number of parameters is $d = 3NL$.

The RPA begins with a fixed layer of $R_Y(\pi/4)$ gates applied to all qubits, followed by a layer of randomly chosen single-qubit Pauli rotations and a fixed sequence of CZ gates. This construction aims to approximate a unitary t -design, introducing sufficient randomness for statistical benchmarking. A general expression for $U(\boldsymbol{\theta})$ in the RPA can be written as

$$U(\boldsymbol{\theta}) = \prod_{\ell=1}^L \left(U_{\text{ent}}^{(\ell)} \cdot U_{\text{ran}}^{(\ell)}(\boldsymbol{\theta}^{(\ell)}) \right) \cdot \left(\bigotimes_{j=1}^N R_Y^{(j)} \left(\frac{\pi}{4} \right) \right), \quad (6)$$

where $U_{\text{ran}}^{(\ell)}(\boldsymbol{\theta}^{(\ell)}) = \bigotimes_{j=1}^N R_{P_j}(\theta_j^{(\ell)})$ and $P_j \in \{X, Y, Z\}$ is a randomly selected Pauli operator for each qubit j , i.e., $R_{P_j}(\theta_j) = \exp\left(-i\frac{\theta_j}{2}P_j\right)$ is a rotation around the Pauli axis P_j by angle θ_j . The total number of parameters is $d = NL$. This ansatz is shallow but introduces sufficient randomness to study expressibility and trainability, while allowing analytical studies on gradient statistics and BPs.

B. Cost function

In VQAs, the cost function is commonly written as [1]

$$C(\boldsymbol{\theta}) = \sum_k f_k \left(\text{Tr}[O_k U(\boldsymbol{\theta}) \rho_k U^\dagger(\boldsymbol{\theta})] \right), \quad (7)$$

where ρ_k denote input quantum states (such as data-encoded states or initial states), O_k are Hermitian observables representing measurement operators or problem-specific Hamiltonians, and f_k are functions applied to the expectation values. This formulation is sufficiently general to encompass a wide range of VQAs,

including those for optimization, simulation, and quantum machine learning, by appropriately choosing ρ_k , O_k , and f_k .

For instance, in VQEs, O_k correspond to the system Hamiltonian H , which can be written as a linear combination $H = \sum_k c_k H_k$, where each H_k is a tensor product of Pauli operators and c_k are real coefficients.

For benchmarking, we optimize the expectation value of a given Hamiltonian, such as $H = Z_1 Z_2$, where Z_j denotes the Pauli-Z operator acting on the j -th qubit [2]. Although this Hamiltonian does not represent a computationally hard problem, it serves the purpose of providing a VQE that has BPs, which allows us to analyze the statistical behavior of the gradient and explore ways to mitigate the BPs in the VQE. The cost function, which guides the optimization process, is defined as

$$C(\boldsymbol{\theta}) = \langle 0 | U(\boldsymbol{\theta})^\dagger H U(\boldsymbol{\theta}) | 0 \rangle, \quad (8)$$

where $|0\rangle = |00\cdots 0\rangle$. This cost function measures the expectation value of the Hamiltonian H under the evolved state $U(\boldsymbol{\theta})|0\rangle$. By adjusting $\boldsymbol{\theta}$, the algorithm seeks to minimize $C(\boldsymbol{\theta})$, effectively finding the optimal quantum state which can be considered an approximation for the ground state of H .

C. BPs in one direction

Figure 5 provides numerical evidence of BPs for two ansätze that represent HEA and RPA at a depth $L = 20$, focusing on the θ_1 direction. In both cases, the cost function $C(\boldsymbol{\theta})$ is plotted as a function of θ_1 , with all other parameters fixed at randomly chosen values [Fig. 5(a, b)]. This allows us to visualize the one-dimensional cost function landscape along the θ_1 direction, consistent with gradient calculations where other parameters are held constant.

For small qubit numbers N , the cost function landscape $C(\boldsymbol{\theta})$ shows clear variation with respect to θ_1 , enabling effective gradient-based optimization. As N increases, the landscape becomes increasingly flat, indicating the evolution towards everywhere-flat BPs. Importantly, no localized dip structure develops as we gradually increase N .

Figures 5(c, d) show the statistical distributions of $\partial_{\theta_1} C$, obtained by randomly sampling all parameters in $\boldsymbol{\theta}$ over $[0, 2\pi]$. We generate 100 sample for each N . We observed that the derivative distribution decreases overall while maintaining a nearly constant spread, similar to the inset of Fig. 1(g), where the everywhere-flat BPs exist. The variance $\text{Var}[\partial_{\theta_1} C]$ exhibits exponential decay with slopes of -0.74 (HEA) and -1.15 (RPA). In contrast, the first region of Fig. 1(g) shows the largest derivatives remaining large, while the smallest shrink significantly. This comparison supports the presence of everywhere-flat barren plateaus in the VQE.

The BPs arise from the concentration of measure in high-dimensional Hilbert spaces, where randomly param-

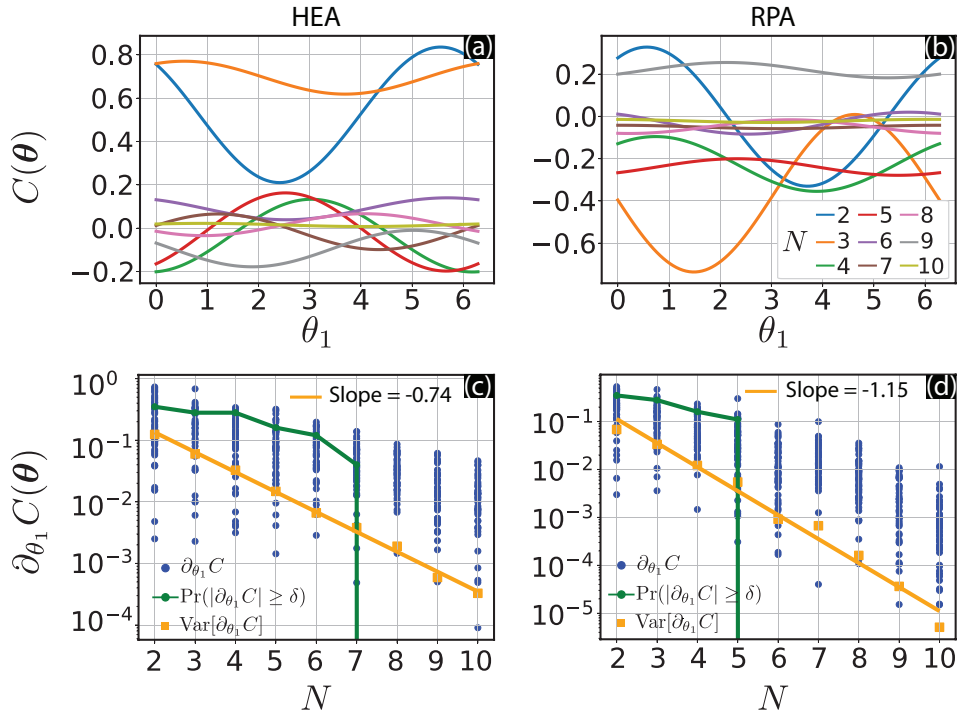


FIG. 5. Numerical analysis of BPs for HEA and RPA with $L = 20$. (a, b) Cost function $C(\theta)$ as a function of θ_1 for various system sizes N , with all other parameters randomly fixed, shown for HEA (a) and RPA (b). (c, d) Derivative distributions $\partial_{\theta_1} C$ under random sampling of $\theta \in [0, 2\pi]$, including the probability $\text{Pr}(|\partial_{\theta_1} C| \geq \delta)$ at $\delta = 10^{-1}$ and the variance $\text{Var}[\partial_{\theta_1} C]$, corresponding to the settings in (a) and (b), respectively and their fitting lines.

eterized circuits yield nearly uniform cost function distributions. Consequently, the cost function becomes insensitive to individual parameter changes, and gradients vanish exponentially with system size. Despite structural differences, both HEA and RPA possess sufficient expressivity and randomness to exhibit this effect even at fixed L .

Furthermore, the probability $\text{Pr}(|\partial_{\theta_1} C| \geq \delta)$ with a threshold $\delta = 10^{-1}$ drops to zero at $N = 7$ and $N = 5$ for two ansätze HEA and RPA, respectively. The specific choice of threshold $\delta = 10^{-1}$ is not intrinsically significant but is chosen to match the gradient scale in our simulations, enabling consistent and meaningful comparisons across ansätze. Using a fixed threshold across different ansätze provides a concrete basis for comparison: a faster decay of this probability reveals an earlier emergence of flat regions in the cost function landscape, indicating a more pronounced BPs.

D. Comparison between different directions in parameter space

We next examine BPs along others parameter directions by analyzing the first six parameters, θ_1 to θ_6 . The results are shown in Fig. 6. For each θ_k , we compute the variance $\text{Var}[\partial_{\theta_k} C]$ over random parameter samples. Exponential decay is observed across all directions, not only

for θ_1 , indicating that the flatness of the cost landscape extends throughout the parameter space.

The slopes vary depending on the parameters. For example, in the HEA in Fig. 6(a), the slopes range from approximately -0.54 to -0.75 , while for RPA in Fig. 6(b), they range from -0.52 to -0.89 . These differences reflect the non-uniform structure of the ansätze but consistently confirm the presence of BPs in all directions.

E. The effect of circuit depth

We now explore how the number of layers L affects the emergence of BPs. The results are shown in Fig. 7. Panels (a) and (b) depict the variance $\text{Var}[\partial_{\theta_1} C]$ as a function of θ_1 for different values of L , using the HEA and RPA ansätze respectively, with system size $N = 2$. In both cases, the variance decreases with increasing L , eventually stabilizing at a limiting value. This behavior is consistent with convergence to an exact 2-design, particularly in the RPA case, where the circuit becomes highly expressive at large depths.

In contrast, for $N = 10$, shown in panels (c) and (d), the trend reverses: the variance increases with L and then saturates. Note that the saturation value is smaller than the one in the $N = 2$ case.

These findings are consistent with previous theoretical studies on the large- L regime, where the variance tends

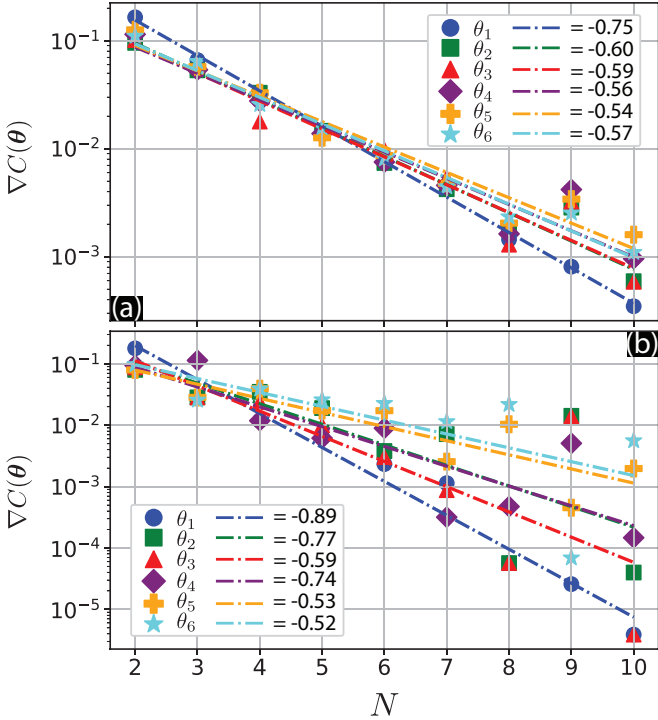


FIG. 6. Absolute values of the first 6 gradients as $\nabla C(\theta) = [|\partial_{\theta_1} C(\theta)|, \dots, |\partial_{\theta_6} C(\theta)|]$ as functions of qubit number N for (a) HEA and (b) RPA.

to a constant that decreases with increasing N [2]. However, we observe a difference at small depths. Specifically, for $N = 10$, the variance remains low when L is small, indicating the presence of BPs in the shallow circuit regime. This highlights that BPs do not develop uniformly across all circuit depths and system sizes. For example, shallow circuits in large systems can maintain negligible gradients.

This behavior can be understood through the statistical concentration of gradients. As established in [2], deeper circuits increasingly resemble random unitary ensembles, eventually forming approximate 2-designs. This leads to gradients approaching zero, characteristic of BPs. However, at shallow depths, the circuit remains far from fully random. Its limited expressivity preserves structure and correlations among parameters, preventing the complete vanishing of gradients.

In our case, when L is small, the circuit lacks sufficient depth to induce full randomization, and gradient distributions remain broad. As L increases, the circuit becomes more expressive, leading to more randomized transformations. This increases the likelihood of gradient suppression due to averaging effects.

IV. BARREN PLATEAU MITIGATION

In this section, we turn to a somewhat different subject. We propose a simple strategy to mitigate the delete-

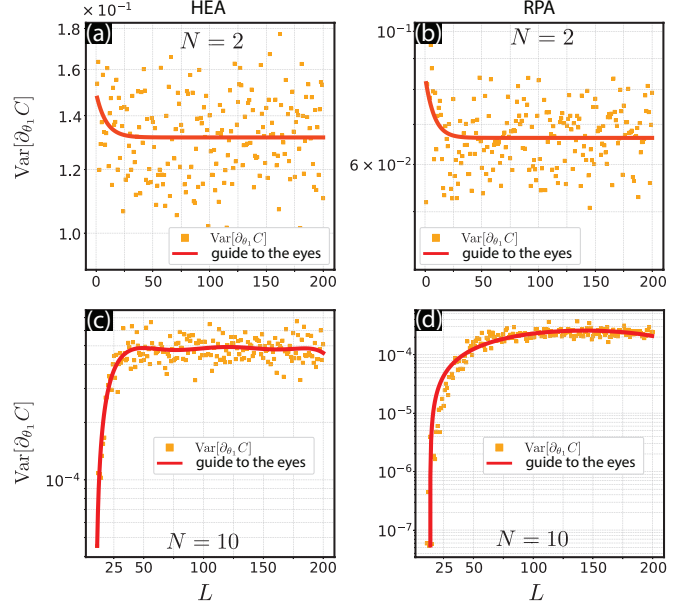


FIG. 7. Variance of the cost function derivative $\text{Var}[\partial_{\theta_1} C]$ as a function of the circuit depths L . Panels (a) and (b) show results for $N = 2$ qubits using the HEA and RPA ansätze, respectively. In both cases, the variance decreases with increasing L , approaching a constant value consistent with the behavior of approximate 2-designs. Panels (c) and (d) display the corresponding results for $N = 10$, where the variance instead increases with L and saturates at an upper bound, indicating a different scaling regime.

rious effects of BPs using a genetic algorithm (GA) [23]. The GA is designed to optimize the randomness of the ansatz. For definiteness, we focus on the RPA and aim to increase the magnitude of its gradient, pushing it away from the zero-gradient regime.

The GA is designed to evolve RPAs into ones that yield large, non-zero gradients. We define the fitness function to an L^p norm objective of the gradient vector $\nabla C(\theta)$ as

$$\mathcal{L} = \|\nabla C(\theta)\|^p = \left(\sum_{i=1}^d |\partial_{\theta_i} C|^p \right)^{1/p}, \quad (9)$$

$$\text{s.t. } \Pr(|\partial_{\theta_i} C| \geq \varepsilon) = 1. \quad (10)$$

where d is the number of parameters, and $\varepsilon > 0$ is a threshold, which can be chosen based on the statistical results of the original ansatz. The condition $\Pr(|\partial_{\theta_i} C| \geq \varepsilon) = 1$ ensures that the gradients for all the parameters in the optimized ansätze will non-vanish. The fitness function \mathcal{L} allows us to compare various generated ansätze and choose the best one.

The GA proceeds as follows: we first generate a set of ansätze. We then evaluate their fitness using the defined fitness function \mathcal{L} . The two highest-scoring ansätze are selected and combined through crossover to produce a new candidate. Crossover refers to exchanging subsets of parameterized gates or circuit layers between two parent circuits to construct a new variational ansatz that inher-

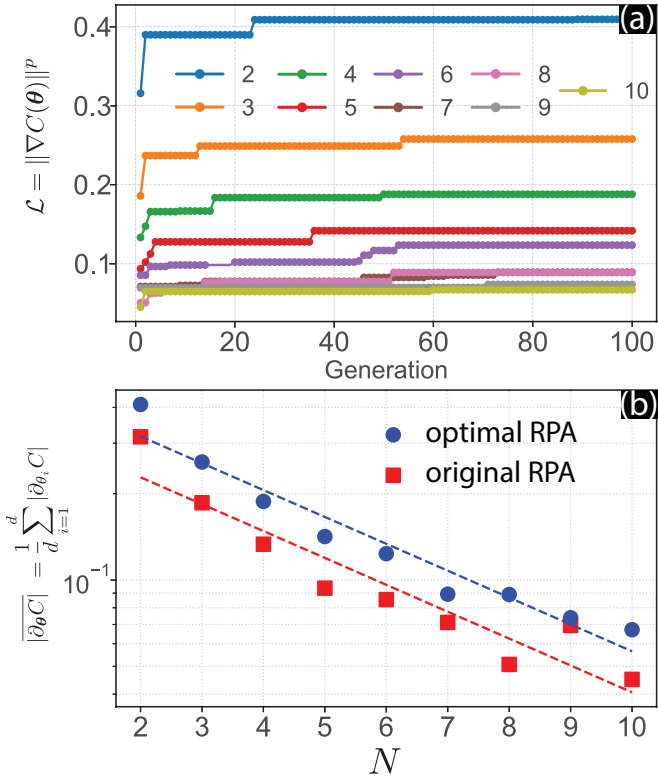


FIG. 8. Numerical analysis of the GA optimization applied to RPAs. (a) Fitness function versus the number of generation for system sizes $N = 2$ to $N = 10$. Initially low fitness values, especially for large N reflect the poor trainability of randomly initialized circuits. As the GA evolves, fitness improves and saturates, indicating successful optimization. (b) Average gradient cost function $\overline{|\partial_{\theta} C|}$ as a function of N , comparing original (unoptimized) RPAs with GA-optimized RPAs. The optimized circuits exhibit significantly higher gradients across all N , confirming improved trainability and suppression of barren plateaus.

its structural features from both. A small mutation is then applied, such as, a random Pauli gate in the circuit is replaced by another Pauli gate with a low but finite probability. The fitness of the new ansatz is evaluated, and the evolution process is repeated either for a fixed number of generations or until the condition (10) satisfy with a certain statistical number of each parameter.

By using the GA optimization, the final ansatz will develop a gradient structure that is non vanishing. During the GA process, the parameters θ are generated randomly, since the objective is to optimize the structure of the ansatz, not the parameter values themselves.

Figure 8 presents the results of the GA optimization. Fig. 8 (a) shows the fitness as a function of the number of generations for system sizes $N = 2$ to $N = 10$ and $p = 1$, $\epsilon = 0.05$. Initially, the RPA circuits are randomly generated, leading to low fitness values, especially for larger N , due to poor gradient flow and a higher likelihood of BPs. As the GA evolves, the fitness improves steadily and eventually saturates, indicating convergence toward

more trainable circuit structures.

Correspondingly, Fig. 8 (b) shows the average gradient cost function, i.e., $\overline{|\partial_{\theta} C|} = \frac{1}{d} \sum_{i=1}^d |\partial_{\theta_i} C|$, plotted against the system size N . We compare two cases: the original (unoptimized) RPA and the optimized RPA obtained via the GA. A clear enhancement in the average gradient is observed for the optimized RPA across all values of N . This improvement reflects the GA's ability to navigate the parameter space and identify circuit architectures that preserve gradient magnitude, thereby mitigating the impact of BPs.

The original case reflects the tendency of randomly initialized deep parameterized quantum circuits to approximate 2-designs, resulting in the emergence of BPs [2]. The GA-based optimization case effectively reshapes the structure of the RPA in the setting where it optimizes and selects only the best candidate among various randomly generated ansätze. As a result, the optimization process actively resists the BPs, especially in the case of larger qubits number. The observed increase in the average $\overline{|\partial_{\theta} C|}$ confirms the enhancement in trainability and supports the effectiveness of the proposed method.

V. CONCLUSION

We developed a statistical framework to analyze BPs in VQAs. By studying an analytically tractable cost function in Gaussian functions, we identified three distinct types of BPs. The first arises near sharp dips or critical points in the parameter space and the second has a sharp gorge. Gradients in these cases are small but still informative, allowing optimization algorithms to make progress. The third, more detrimental type, occurs in uniformly flat regions of the landscape, where gradients vanish across broad domains, significantly impeding trainability.

We then apply the framework to HEA and RPA ansätze in VQE settings, where we found that only the second type of BP appears. To mitigate the BPs in VQE, we proposed a GA-based optimization scheme aimed at reshaping the cost landscape. By selectively enhancing structure and gradient visibility, our method effectively suppresses the occurrence of flat barren plateaus and enables more efficient training, even in larger systems. These findings contribute a new perspective on the barren plateau problem and suggest a practical pathway toward improving the scalability of VQAs.

ACKNOWLEDGMENTS

This paper is supported by JSPS KAKENHI Grant No.23K13025. SA was supported by Japan's Ministry of Education, Culture, Sports, Science and Technology (MEXT) Quantum Leap Flagship Program Grant Number JPMXS0120319794.

[1] M. Cerezo, A. Arrasmith, R. Babbush, S. C. Benjamin, S. Endo, K. Fujii, J. R. McClean, K. Mitarai, X. Yuan, L. Cincio, and P. J. Coles, Variational quantum algorithms, *Nature Reviews Physics* **3**, 625 (2021).

[2] J. R. McClean, S. Boixo, V. N. Smelyanskiy, R. Babbush, and H. Neven, Barren plateaus in quantum neural network training landscapes, *Nature Communications* **9**, 4812 (2018).

[3] M. Cerezo, A. Sone, T. Volkoff, L. Cincio, and P. J. Coles, Cost function dependent barren plateaus in shallow parametrized quantum circuits, *Nature Communications* **12**, 1791 (2021).

[4] Z. Holmes, K. Sharma, M. Cerezo, and P. J. Coles, Connecting ansatz expressibility to gradient magnitudes and barren plateaus, *PRX Quantum* **3**, 010313 (2022).

[5] M. Larocca, P. Czarnik, K. Sharma, G. Muraleedharan, P. J. Coles, and M. Cerezo, Diagnosing Barren Plateaus with Tools from Quantum Optimal Control, *Quantum* **6**, 824 (2022).

[6] A. V. Uvarov and J. D. Biamonte, On barren plateaus and cost function locality in variational quantum algorithms, *Journal of Physics A: Mathematical and Theoretical* **54**, 245301 (2021).

[7] A. Arrasmith, Z. Holmes, M. Cerezo, and P. J. Coles, Equivalence of quantum barren plateaus to cost concentration and narrow gorges, *Quantum Science and Technology* **7**, 045015 (2022).

[8] S. Wang, E. Fontana, M. Cerezo, K. Sharma, A. Sone, L. Cincio, and P. J. Coles, Noise-induced barren plateaus in variational quantum algorithms, *Nature Communications* **12**, 6961 (2021).

[9] C. Ortiz Marrero, M. Kieferová, and N. Wiebe, Entanglement-induced barren plateaus, *PRX Quantum* **2**, 040316 (2021).

[10] M. Ragone, B. N. Bakalov, F. Sauvage, A. F. Kemper, C. Ortiz Marrero, M. Larocca, and M. Cerezo, A lie algebraic theory of barren plateaus for deep parameterized quantum circuits, *Nature Communications* **15**, 7172 (2024).

[11] E. Fontana, D. Herman, S. Chakrabarti, N. Kumar, R. Yalovetzky, J. Heredge, S. H. Sureshbabu, and M. Pistoiia, Characterizing barren plateaus in quantum ansätze with the adjoint representation, *Nature Communications* **15**, 7171 (2024).

[12] H.-Y. Liu, T.-P. Sun, Y.-C. Wu, Y.-J. Han, and G.-P. Guo, Mitigating barren plateaus with transfer-learning-inspired parameter initializations, *New Journal of Physics* **25**, 013039 (2023).

[13] E. Grant, L. Wossnig, M. Ostaszewski, and M. Benedetti, An initialization strategy for addressing barren plateaus in parametrized quantum circuits, *Quantum* **3**, 214 (2019).

[14] T. Volkoff and P. J. Coles, Large gradients via correlation in random parameterized quantum circuits, *Quantum Science and Technology* **6**, 025008 (2021).

[15] T. L. Patti, K. Najafi, X. Gao, and S. F. Yelin, Entanglement devised barren plateau mitigation, *Phys. Rev. Res.* **3**, 033090 (2021).

[16] S. H. Sack, R. A. Medina, A. A. Michailidis, R. Kueng, and M. Serbyn, Avoiding barren plateaus using classical shadows, *PRX Quantum* **3**, 020365 (2022).

[17] A. A. Mele, G. B. Mbeng, G. E. Santoro, M. Collura, and P. Torta, Avoiding barren plateaus via transferability of smooth solutions in a hamiltonian variational ansatz, *Phys. Rev. A* **106**, L060401 (2022).

[18] L. Friedrich and J. Maziero, Avoiding barren plateaus with classical deep neural networks, *Phys. Rev. A* **106**, 042433 (2022).

[19] J. Dborin, F. Barratt, V. Wimalaweera, L. Wright, and A. G. Green, Matrix product state pre-training for quantum machine learning, *Quantum Science and Technology* **7**, 035014 (2022).

[20] L. Liu, T. Song, Z. Sun, and J. Lei, Quantum generative adversarial networks based on rényi divergences, *Physica A: Statistical Mechanics and its Applications* **607**, 128169 (2022).

[21] M. Kieferová, O. M. Carlos, and N. Wiebe, Quantum generative training using rényi divergences (2021), arXiv:2106.09567 [quant-ph].

[22] A. Sannia, F. Tacchino, I. Tavernelli, G. L. Giorgi, and R. Zambrini, Engineered dissipation to mitigate barren plateaus, *npj Quantum Information* **10**, 81 (2024).

[23] V. Tuan Hai, N. Tan Viet, J. Urbaneja, N. Vu Linh, L. Nguyen Tran, and L. Bin Ho, Multi-target quantum compilation algorithm, *Machine Learning: Science and Technology* **5**, 045057 (2024).

[24] A. Peruzzo, J. McClean, P. Shadbolt, M.-H. Yung, X.-Q. Zhou, P. J. Love, A. Aspuru-Guzik, and J. L. O'Brien, A variational eigenvalue solver on a photonic quantum processor, *Nature Communications* **5**, 4213 (2014).

[25] A. Kandala, A. Mezzacapo, K. Temme, M. Takita, M. Brink, J. M. Chow, and J. M. Gambetta, Hardware-efficient variational quantum eigensolver for small molecules and quantum magnets, *Nature* **549**, 242 (2017).